Applied Physics A (2023) 129:380
https://doi.org/10.1007/s00339-023-06663-5

Applied Physics A
Materials Science & Processing

Fabrication of MoS_2/Bi_2S_3 heterostructure for photocatalytic degradation of Metronidazole and Cefalexin and antibacterial applications under NIR light: experimental and theoretical approach

Hoda Pasdar[1] · Narges Elmi Fard[2] · Mahyar Rezvani[3]

Received: 6 January 2023 / Accepted: 17 April 2023 / Published online: 26 April 2023

Abstract

In this research, molybdenum disulfide (MoS_2) and bismuth trisulfide (Bi_2S_3) particles were synthesized. Bi_2S_3 was loaded on MoS_2 nanosheet and was characterized by several techniques. Degradation of metronidazole (MTZ) and Cefalexin (CFX) were investigated via MoS_2, Bi_2S_3, and MoS_2/Bi_2S_3 particles under near-infrared (NIR) light irradiation. The evaluations of electronic structures and molecular geometries of MoS_2 monolayer, MoS_2/MTZ, and MoS_2/CFX complexes were implemented using the DFT method. According to the electronic density of states (DOS) graphs results, when the MTZ and CFX interact with the monolayer surface, the energy gap (E_g) decreases compared to the MoS_2 nanosheet. In other words, the electronic features of the MoS_2 monolayer were altered after interaction with MTZ and CFX, where a reduction in the E_g value was evaluated (from 1.973 eV in the bare MoS_2 to 0.010 and 1.936 eV in states MTZ and CFX complexes, an alteration of 99.49 and 1.875%, respectively. It can be concluded that the band gap significantly changes when the MTZ interacts with the monolayer surface. The maximum removal efficiencies of MTZ and CFX in 40 min and at pH 7 were obtained by MoS_2/Bi_2S_3 photocatalyst, 91.54 and 73.18%, respectively. The results showed that the particles of Bi_2S_3, MoS_2, and MoS_2/Bi_2S_3 under NIR light irradiation have antibacterial properties, and the highest antibacterial property is related to the MoS_2/Bi_2S_3 particles.

Graphical abstract

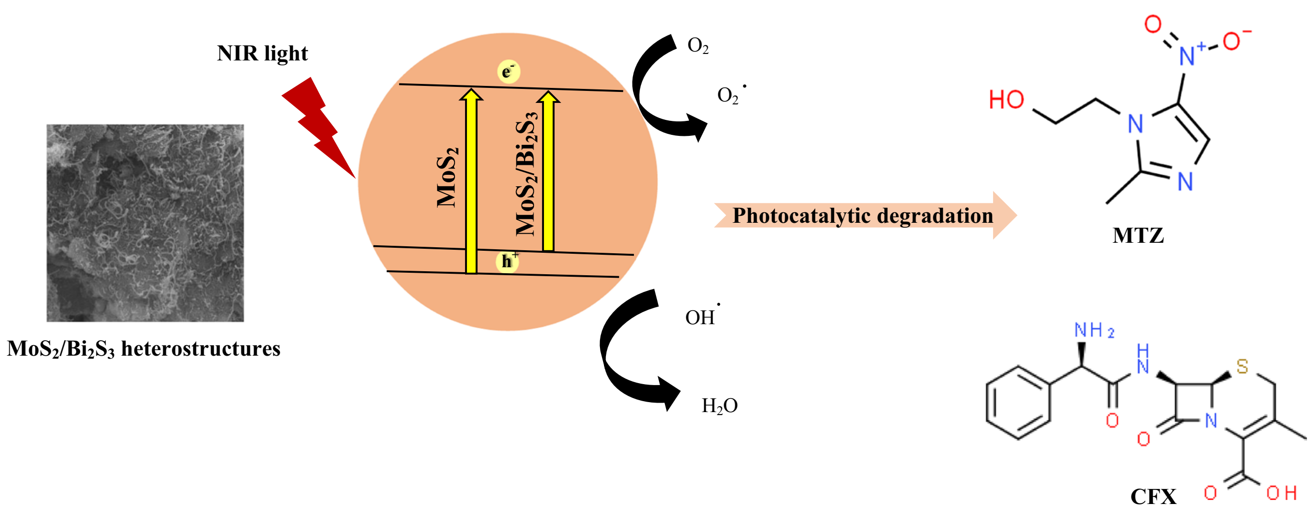

Keywords MoS_2/Bi_2S_3 · Photocatalyst · Degradation · MTZ · CFX · DFT

✉ Hoda Pasdar
H_pasdar@iau-tnb.ac.ir

Extended author information available on the last page of the article

1 Introduction

Pollutants in the pharmaceutical industry wastewater treatment are very complex, non-biodegradable, and very harmful to the environment [1, 2]. The most important effect of antibiotics is low biological biodegradability, high toxicity, specific carcinogenicity, and most importantly their lack of biodegradability, and mutagenic. Their entry into municipal wastewater treatment plants can cause the death of treated organisms and disrupt biological treatment systems [3, 4]. Metronidazole (MTZ) with anti-inflammatory and antibacterial properties is one of the most widely used antibiotics in the world [5]. Its applications include the treatment of infectious diseases caused by anaerobic bacteria and protozoa and its use as an antiparasitic in poultry and fish [6]. This antibiotic is due to its high potency in eliminating infections of the gastrointestinal tract, mouth, teeth, and genitals in the affected organ, and it is one of the most widely used drugs [7, 8].

Cefalexin (CFX) is a cephalosporin antibiotic that is effective in treating many groups of infectious diseases, such as respiratory infections, middle ear infections, skin and soft tissue infections, bone or joint infections, and urinary and genital infections [9]. It is also used for people who have had surgery and other people who are prone to infection for any reason. Therefore, its presence in household effluents, hospitals, and pharmaceutical industries is high. Therefore, these widely used antibiotics must be treated before entering the environment [10]. Various techniques, such as membrane, oxidation, solid phase extraction, sonochemical degradation, nanofiltration, and electrophoresis, have been performed. Advanced oxidation processes (AOPs), including photocatalytic methods [11–20], have shown good potential for the removal of biodegradable organic compounds from municipal and industrial wastewater [21]. Due to the properties of MTZ and CFX antibiotics, it is necessary to control and eliminate this contaminant. In recent years, a family of chemical compounds known as dichalcogen-mediated metals, which have shown interesting properties, have received much attention [22].

MOS_2 is part of the family of dicalcogen intermediate metals. Unlike graphene, these materials offer a variety of electronic properties [23]. As the most famous member of the family of intermediate dicalcogenes, MoS_2 has been extensively used in two-dimensional fields in various fields, such as biomedicine, sensing, catalytic, antibacterial, and field-effect transistors [24]. Recently, the use of MoS_2 nanostructures as an adsorbent in aqueous solution, especially with the nanosheet structure, has received a lot of attention [25]. MoS_2 as a p-type semiconductor band gap is shown to change from 1.9 to 2.8 eV by the dielectric environment [26, 27]. Meanwhile, the preparation of MoS_2 nanostructures by various methods of preparing nanostructures in parallel with their application has received much attention. One of the most optimal methods for the production of nanostructures is the hydrothermal method [28].

Bismuth trisulfide (Bi_2S_3) as an n-type has gained considerable attention because of its nontoxicity, low cost, direct band gap ($E_g = 1.1$ and 1.6 eV), thermo-chemical stability, and good optoelectronic and thermoelectric properties. Bi_2S_3 is a layered semiconductor with an orthorhombic crystal structure [29, 30]. The applications of Bi_2S_3 include areas, such as solar cells, sensors, photodetectors, photocatalysis, antibacterial, and thermoelectric devices [31]. Bi_2S_3 has different morphologies, such as flower, wire, tube, and sphere [32]. Various methods are used for synthesis such as microwave, hydrothermal, and solvothermal. Semiconductors have conduction between the conductor and the insulator [33].

P-n junctions are very simple bonds with a p-type semiconductor compound on one side of the bond and an n-type semiconductor compound on the other side [34]. In n-type matter, electrons increase, and in p-type, holes predominate. In type n semiconductors, the number of electrons is much more than the number in p-type semiconductors, and also in type p semiconductors, the number of holes is much more than the number in n-type semiconductors. For this reason, when the two types of semiconductors n and p are connected to each other, electrons penetrate into the semiconductor p and holes penetrate into the semiconductor n. The penetration of an electron from the n region to the p region causes the formation of a positive ion in the n-type semiconductor and also similarly, the penetration of a hole causes a negative ion acceptor to form in the p region. It recombines with one of the holes on the p side [35].

Sulfide semiconductors with a small band gap have high photocatalytic activity by starting absorption in the visible and NIR regions. Due to synergy, MoS_2/Bi_2S_3 particles have a higher reactive oxidation species (ROS) production capacity and more antibacterial properties [36].

This research aims to investigate the removal of commonly used MTZ and CFX antibiotics using MoS_2, Bi_2S_3, and MoS_2/Bi_2S_3 photocatalysts under NIR irradiation. Furthermore, the antibacterial activity of MoS_2, Bi_2S_3, and MoS_2/Bi_2S_3 photocatalysts under NIR irradiation and in the dark has been studied. To compare the experimental and theoretical results, electronic structures and molecular geometries of MoS_2 monolayer, MoS_2/MTZ, and MoS_2/CFX complexes were implemented using the DFT method.

2 Materials and methods

2.1 Material

Ammonium heptamolybdate tetrahydrate ($(NH_4)_6Mo_7O_{24}$, ≥ 99%), thiourea (CH_4N_2S, > 99%), and bismuth nitrate $Bi(NO_3)$ from Sigma-Aldrich company was prepared. Metronidazole ($C_6H_9N_3O_3$) and Cefalexin ($C_{16}H_{17}N_3O_4S$) antibiotics were purchased by Darou Pakhsh Company.

2.2 Synthesis of MoS_2

First, 1.24 g of $(NH_4)6Mo_7O_{24}$ and 2.28 g of CH_4N_2S were poured into 36 mL of distilled water and stirred for 30 min. The resulting solution was poured into an autoclave stainless steel for 7 h at a temperature of 170 °C. After performing the synthesis process, a precipitate is obtained which was washed several times with distilled water, and heated in an oven at 150 °C for 2 h to give the MoS_2 product [28].

2.3 Synthesis of Bi_2S_3

0.25 g of CH_4N_2S and 0.61 g of bismuth nitrate $Bi(NO_3)$ were poured in 50 mL of distilled water and stirred for 30 min. Then, 5 mL of HCl was added to the solution. The resulting solution was poured into an autoclave for 20 h at 140 °C. After performing the synthesis process, a precipitate obtained was washed several times with distilled water [37].

2.4 Synthesis of MoS_2/Bi_2S_3

MoS_2/Bi_2S_3 photocatalyst was prepared with a weight ratio of 1:1. In this way, first 0.05 g of MoS_2 and 0.05 g of Bi_2S_3 were poured into 100 mL of distilled water and stirred for 12 h at room temperature. The mixture was washed and dried at 60 °C for 6 h and was placed in a furnace at 400 °C for 3 h.

2.5 Degradation of MTZ and CFX

In this step, MTZ and CFX were prepared at a concentration of 100 mg/L at pH 7. The amount of 0.02 g of MoS_2, Bi_2S_3, and MoS_2/Bi_2S_3 was added to 50 mL of prepared drugs and placed on a magnetic stirrer exposed to NIR light (800 nm, 100 W/cm^2) for 5–45 min. Then, the samples were centrifuged at 7500 rpm for 15 min. Finally, the absorption of MTZ and CFX was measured by spectrophotometer at 319 and 261 nm, respectively

$$\text{Efficiency} = \frac{(A_0 - A_t)}{A_0} \times 100, \quad (1)$$

where A_0 is the initial adsorption of the drugs and A_t is its final adsorption on the photocatalytic degradation [20].

2.6 MoS_2/Bi_2S_3 photocatalyst recycling

For this purpose, the MoS_2/Bi_2S_3 photocatalyst used in the degradation process of MTZ and CFX antibiotics was collected by centrifugation and then washed once with ethanol and three times with distilled water. The collected photocatalyst was dried at ambient temperature and then the photocatalyst was reused in the degradation reaction of MTZ and CFX antibiotics.

2.7 Computational details

The evaluations of electronic structures and molecular geometries of MoS_2 monolayer and MTZ/CFX were implemented by means of the DFT method [38, 39] using SIESTA simulation software [40, 41]. Conventional DFT technics do not discuss long-range attractive contributions to van der Waals (vdW) interactions between the adsorbent and adsorbate. Therefore, the dispersion-corrected DFT combined with generalized gradient approximation (GGA-PBE) [42] approaches were employed [43–46]. The PBE function is a good choice for studying MoS_2 material, which is confirmed by the reported DFT work [47]. In the simulation, a two-dimensional periodic boundary condition was utilized for the super-cells with 15.75 × 13.64 × 25 Å for the MoS_2 monolayer. The double zeta polarization (DZP) orbitals have been utilized for the relaxation of the MoS_2 nanosheet in the present study [48]. Furthermore, the interaction between the nuclei and core electrons and the valence electrons was estimated via Troullier–Martin realistic scheme [49, 50]. Further, the complete geometrical optimization was carried out with a conjugate gradient (CG) algorithm until the Hellmann–Feynman force including Pullay-like corrections was converged to 0.01 eV/Å [51]. The mesh cutoff was set to 150 Ry which presents a good accuracy. To better comprehension of physical quantities, a Brillouin zone was sampled using Monkhorst–Pack 5 × 5 × 1 k point sampling for converging geometry, whereas 15 × 15 × 1 for the assessment of the electronic DOS and charge transfer (CT) analysis [52]. The unit cell is allowed to converge in *xy* directions, whereas the *z* path is kept frozen at 25°A, consequently to eschew unwanted interactions between replicas.

To calculate the binding features of MoS_2/Drugs complexes, we computed the interaction energies via pseudopotential approach through van der Waals (vdW) correction suggested by Grimme (DFT-D2) scheme [53] as well applied OpenMX code which is an outstanding DFT code for evaluating the molecular systems [54, 55]. The numerical pseudo-atomic orbitals' (PAOs) method was employed as the basis sets for the Kohn–Sham potential and orbitals [56]. PAO basis functions are specified by C-s2p2d1, H 5.0-s2p2d1, N-s2p2d1, O 7.0-s2p2d1, S 7.0-s2p2d1, and Mo 7.0-s2p2d1. The energy cutoff for MoS_2/Drugs was selected at 200 Ry [57]. In structural optimizations, convergence was assumed around 10^{-4} Hartree/Bohr, which offers rational outcomes for under study complexes.

The interaction energy as called E_{int} for the interacting Drugs with the MoS_2 is defined as

$$E_{int} = E\left(\frac{MoS_2}{Drugs}\right) - \left[E\left(MoS_2\right) + E(Drugs)\right] - \delta_{BSSE}, \quad (2)$$

where E (MoS_2/Drugs), E (MoS_2), and E (Drugs) are the total energies of the relaxed MoS_2/Drugs complex, the pure MoS_2, and the isolated drugs, respectively.

It is worth mentioning that the basis set superposition error (BSSE) correction was utilized through the counterpoise correction (CC) approach [56]. The δ_{BSSE} statement corresponds to the corrections on the BSSE using the counterpoise technique.

Besides, to clarify the electronic sensitivity of the MoS_2 monolayer toward the adsorption of the drug, the modification in E_g is assessed by

$$\Delta Eg = \left[\frac{(Eg2 - Eg1)}{Eg1}\right] \times 100\%, \quad (3)$$

where E_{g1} and E_{g2} are the measures of E_g for the pure MoS_2 and the drugs, respectively.

To investigate the nature of the interaction between drugs and MoS_2, the CT was considered through the Mulliken technique [58, 59].

2.8 Antibacterial activities

In this method, each sterilized disk was loaded with a different solution of Bi_2S_3, MoS_2, and MoS_2/Bi_2S_3 particles at a concentration of 1000 mg/μL. The dried disks are then placed on the surface of the NA agar plates sprayed uniformly by ca 1×10^6 CFU/ml of *Escherichia coli* (*E. coli*) from the culture medium by the applicator and inoculated into the culture medium. Plates with no treatments were used as control. Petri dishes were then irradiated with NIR light (800 nm, 100 W/cm^2) for 2 min and also without light and incubated at 37 °C for 12 h in a shaking incubator. After 12 h, the diameters of the growth halos created around the disks were measured in millimeters with a caliper.

3 Results and discussion

3.1 Characterization

XRD technique was used to identify the phase and structure of MoS_2 and Bi_2S_3, MoS_2/Bi_2S_3 photocatalysts. Figure 1 shows the XRD pattern of samples. The XRD of MoS_2 at the angles of 14.39, 32.91, 39.69, and 76.58° corresponds to plates (002), (100), (103), and (110), respectively; which indicates the hexagonal phase by the standard peaks of the characteristic MoS_2 with JCPDS card No. 00-037-1492. The XRD spectrum of the Bi_2S_3 at the angles of 25.01, 28.66, 32.46, and 46.51° corresponds to plates (101), (130), (021), and (431), respectively. The results showed that the Bi_2S_3 were crystallized orthorhombic phase with the value in standard JCPDS card No. 00-017-0320. The peaks of MoS_2/Bi_2S_3 at angles 14.39, 32.91, 39.69, and 76.58° are related to MoS_2, and the peaks at angles of 25.01, 28.66, 32.46, and 46.5°, are related to Bi_2S_3, respectively (Fig. 1).

The average particle size was estimated based on the Debye–Scherrer equation using X'pert Highscore software

$$B = \frac{K\lambda}{L\cos\theta}, \quad (4)$$

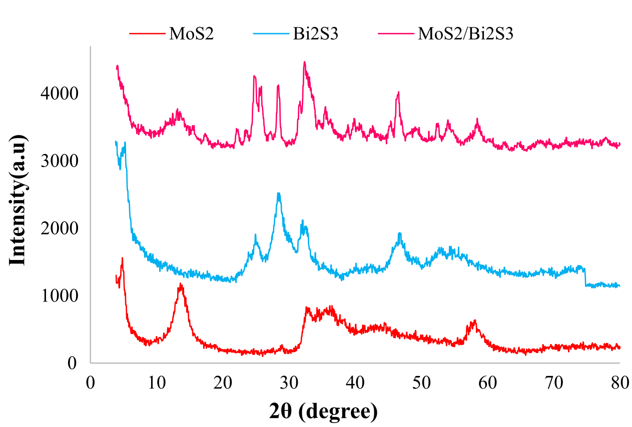

Fig. 1 XRD spectra obtained for MoS_2, Bi_2S_3, and MoS_2/Bi_2S_3

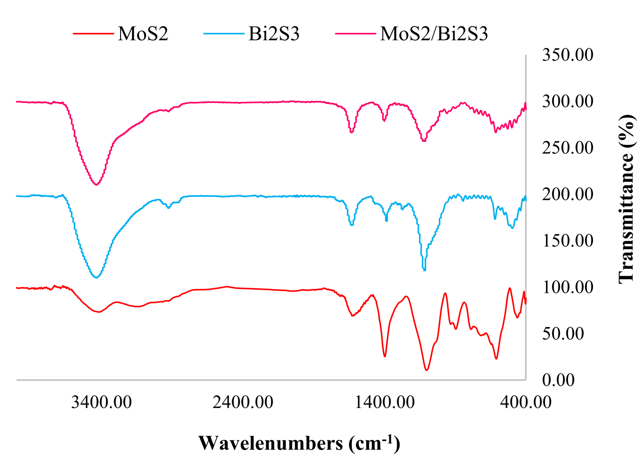

Fig. 2 FTIR spectra obtained for MoS_2, Bi_2S_3, and MoS_2/Bi_2S_3

Table 1 Calculated crystalline and lattice parameters for MoS_2 and Bi_2S_3

Sample	*B* (nm)	Space group	*a* (Å)	*b* (Å)	*c* (Å)
MoS_2	52.67	P63/mmc	3.1612	3.1612	12.2985
Bi_2S_3	29.95	Pbnm	11.1490	11.3040	3.9810

where *B* is the particle size, *K* is a constant number equal to 0.9, λ is the applied wavelength in terms of nanometers, and *L* is the peak full width at half maximum (FWHM) in terms of radians and θ is the angle corresponding to the highest peak [20].

The mean particle sizes calculated by the Debye–Scherrer method were MoS_2, Bi_2S_3, and MoS_2/Bi_2S_3 52.67 and 29.95, and 64.71 nm, respectively.

For the synthesized particles, the calculated crystal and lattice parameters are displayed in Table 1.

The interaction of infrared radiation with a sample changes the vibrational energy of the bond in its molecules and is a good way to identify functional groups and molecular structures. The FTIR spectra of the MoS_2 in the range

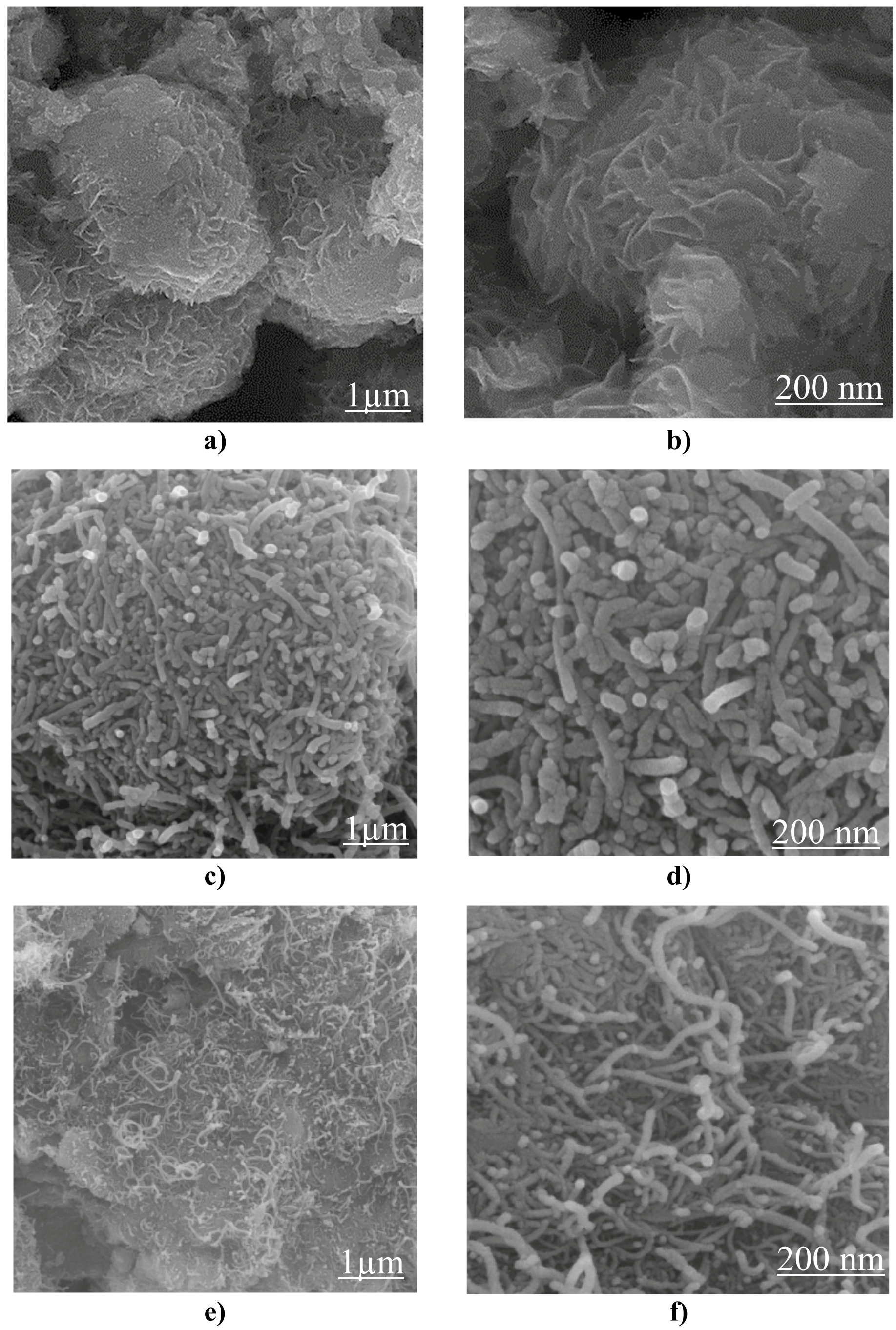

Fig. 3 SEM images, **a**, **b** MoS_2, **c**, **d** Bi_2S_3, and **e**, **f** MoS_2/Bi_2S_3

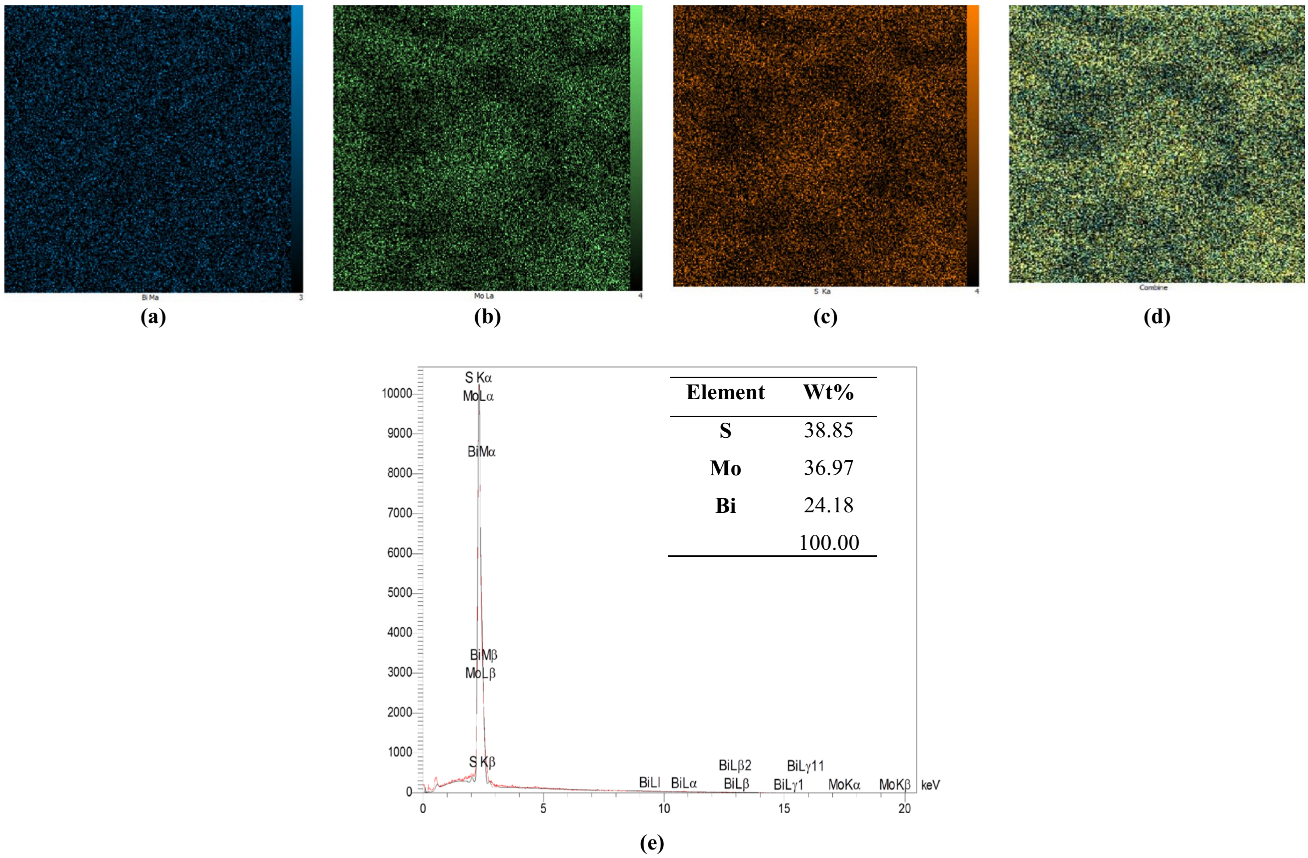

Fig. 4 Map images of **a** Bi, **b** Mo, **c** S, **d** combine and **e** EDS pattern of MoS_2/Bi_2S_3

of 476.29 cm^{-1} are related to the Mo–S tensile vibration and in the peak range of 3424.21 cm^{-1} assigned to the O–H tensile vibration. The spectra of FTIR Bi_2S_3 in the range of 495.36 cm^{-1} are related to the tensile vibration of Bi–O, in the range of 618.16 cm^{-1} characteristic to C–S bond, and the peak located at 1117.73, 1271.87 and 2924.92 cm^{-1} corresponds to the bending vibration C–O, C–O–C, and C–H bond. Also, in the peak range 3436.05 cm^{-1}, it is related to O–H tensile vibration (Fig. 2). In the MoS_2/Bi_2S_3, the absorption bands at 467.93, 499.04, 528.85, and 613.33 cm^{-1} are assigned to the Mo–S, Bi–O, C–S, and C–S. The peak located at 1113.29, 1400.97, and 1631.65 cm^{-1} corresponds to the bending vibration C–O, C–S, and H–O–H bond. Also, in the peak range of 3436.05 cm^{-1}, it is related to O–H tensile vibration (Fig. 2).

SEM technique was used to determine the surface characteristics and morphology of the synthesized particles. Based on the morphological results, MoS_2 is like flower, Bi_2S_3 is Rod, and Bi_2S_3 particles are well stabilized on MoS_2 (Fig. 3).

Based on the EDS diagram, Mo (36.97%), Bi (24.18%), and S (38.85%) elements are present in MoS_2/Bi_2S_3. The Xmap technique examines point-by-point a specific area of the sample. In this technique, EDS analysis is performed from a large number of points in a specified area and the results of this analysis are displayed as a series of colored dots. Each color represents an element. Where the amount of this element is greater, the number of dots with that particular color is greater. In the Map images for MoS_2/Bi_2S_3 the blue, green, and orange dots represent the presence of Bi, Mo, and S, respectively (Fig. 4).

BET/BJH results of MoS_2, Bi_2S_3, and MoS_2/Bi_2S_3 samples are shown in Fig. 5. Based on the results, by loading the Bi_2S_3 rod on MoS_2 flower surface area and total pore volume increased. However, the average diameter of the average cavities decreased, which shows that Bi_2S_3 is well loaded on MoS_2 (Table 2).

Using the absorption coefficient (α), the band gap of thin layers can be studied with the help of the Tauc equation [16]

$$(\alpha h\nu)1/n = A\left(h\nu - E_g\right), \quad (5)$$

where h is the Planck constant, ν is the applied frequency, α is the absorption coefficient, E_g is the band gap, and A is a proportional constant. The band-gap values for MoS_2, Bi_2S_3, and MoS_2/Bi_2S_3 1.90, 1.18, and 1.79 (eV) were determined

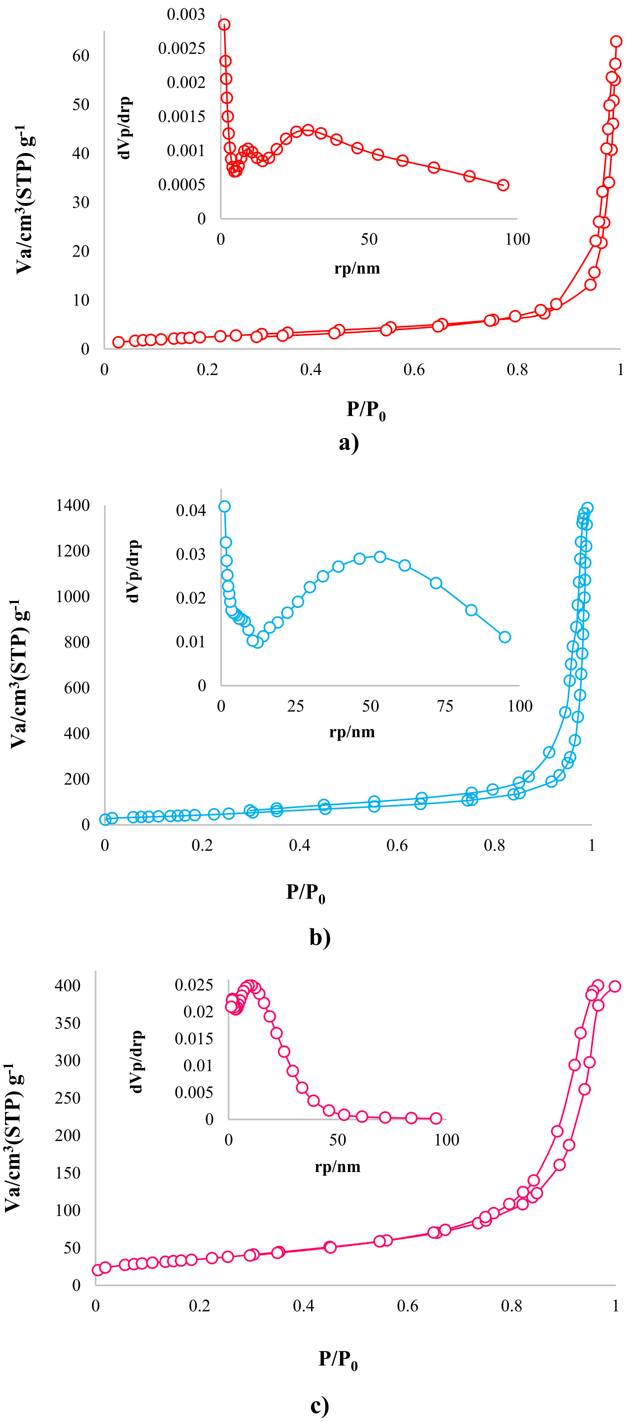

Fig. 5 BET/BJH analysis for **a** MoS_2, **b** Bi_2S_3, and **c** MoS_2/Bi_2S_3

by the Tauc method. The Tauc diagram is shown in Fig. 6. Based on the results as the MoS_2 was bound to Bi_2S_3, the band gap decreased.

Table 2 BET/BJH results for MoS_2, Bi_2S_3, and MoS_2/Bi_2S_3

Sample	a_S, BET ($m^2\ g^{-1}$)	Total pore volume ($cm^3\ g^{-1}$)	Mean pore diameter (nm)
MoS_2	9.67	10.58	37.60
Bi_2S_3	151.96	2.03	54.82
MoS_2/Bi_2S_3	125.72	8.41	44.29

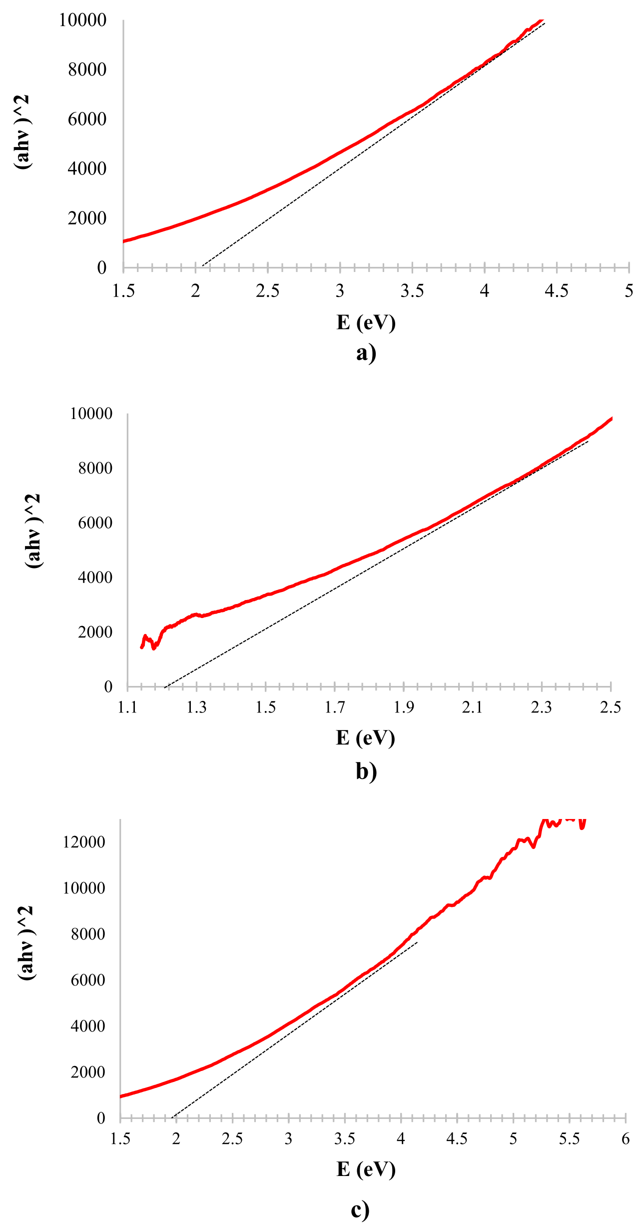

Fig. 6 Band gap energies of **a** MoS_2, **b** Bi_2S_3, and **c** MoS_2/Bi_2S_3

Table 3 The calculated Mo–S, S–S distances (Å), and gap energy (E_g) for MoS_2 structure as calculated theoretical works

Method	d_{Mo-S} (Å)	d_{S-S} (Å)	E_g (eV)	References
GGA-PBE	2.42	3.17	1.973	This work
GGA-RPBE	2.43	3.18	1.986	[60]
GGA-PW91	2.41	–	1.690	[61]
GGA-PW91	2.43	3.18	1.650	[62]
B88-vdW/USP	2.43	3.15	1.900	[63]
PBE-D2/USP	2.42	3.12	1.900	[63]

3.2 Theoretical section

In this section, we examine the interaction between the MoS_2 monolayer and selected drugs in the aqueous environment. In our calculations, MoS_2 monolayer with 17.75 Å × 13.64 Å super-cells has been modeled consisting of 25 and 50 molybdenum and sulfur atoms, respectively. The converged structure of the MoS_2 has a Mo−S bond length of around 2.42 Å. The separation between sulfur layers evaluated as 3.17 Å allows for direct comparison to the experimental data, 3.18 Å, calculated through STM images (Table 3). The obtained results are in good agreement with theoretical outcomes [60–63]. To discover the most stable structure of MET/CEPH drugs interacting with MoS_2 monolayer, the GGA-PBE approach was implemented for optimization and DFT-D2 for total energies calculations of above-mentioned systems. According to the main goal in this study is the elimination of mentioned drugs in industrial wastewater, we performed the drugs and MoS_2 monolayer interaction in the presence of water molecules as denoted in Fig. 7. After the optimization of the initial structures, the E_{int} were calculated with the DFT−D2 scheme. The E_{int} were assessed around − 1.306 and − 1.060 eV for MTZ and CFX, respectively, as presented in Table 4. Simultaneously, we considered equilibrium distances in MoS_2/Drugs complex. The obtained results reveal that the distance between the S atom of the MoS_2 monolayer and the H atoms of CFX and MTZ is 2.507 and 2.513 Å, respectively (Fig. 8). Charge analysis is a vital analysis to consider the intermolecular and intra-molecular interactions, and as an appropriate source

Table 4 The detail data of adsorption: adsorption energy (Eb), adsorption distance (*D*), and Mulliken charge transfer (*e*)

Configuration	Eb (DFT-D2)	*D* (A°)	Mulliken (*e*)
MoS_2/MTZ	− 1.306	2.513	0.121
MoS_2/CFX	− 1.060	2.507	0.010

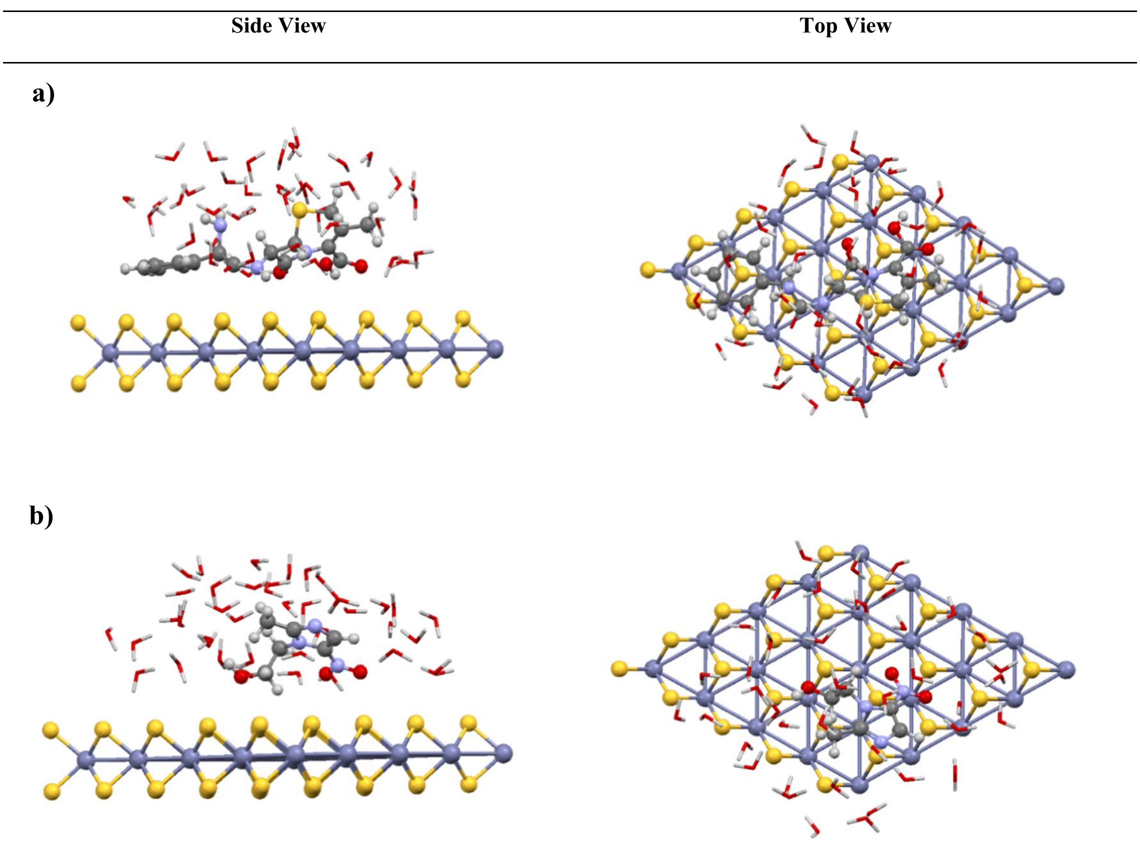

Fig. 7 Optimized configurations of interactions between **a** MTZ, **b** CFX, and MoS_2 monolayer with DFT level of theory

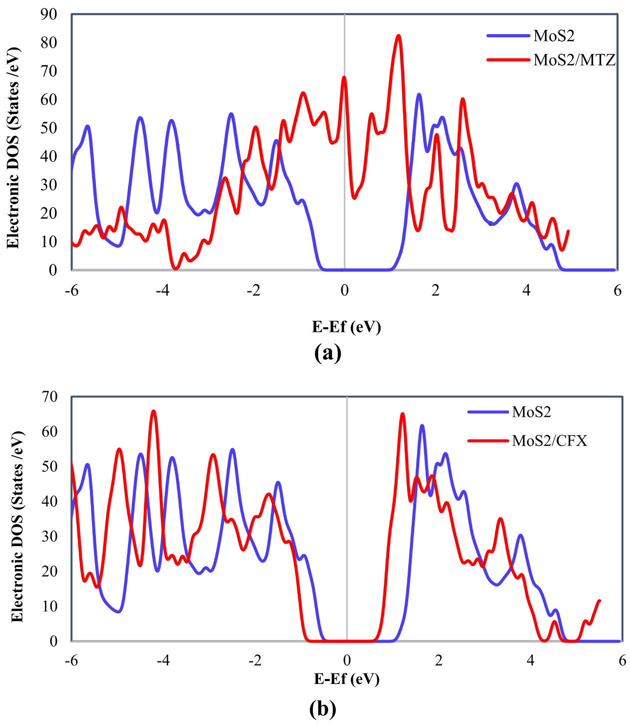

Fig. 8 DOS curves of **a** CTZ-MoS_2 and **b** CFX-MoS_2 compared with pure MoS_2 monolayer. The dotted lines are Fermi level

Table 5 Computed E_{HOMO}, E_{LUMO}, E_g, E_F (in eV) and ΔE_g is change of E_g, for MoS_2/MTZ, MoS_2/CFX complexes and pure MoS_2, Bi_2S_3

Configuration	E_{HOMO}	E_{LUMO}	E_g	E_F	ΔE_g %
MoS_2	−4.637	−2.664	1.973	−3.926	–
Bi_2S_3	−3.740	−2.606	1.134	−3.186	–
MoS_2/MTZ	−2.922	−2.912	0.010	−2.915	99.49
MoS_2/CFX	−4.578	−2.642	1.936	−3.502	1.875

for the investigation of the charge transferring in molecular systems. In this stage of the investigation, we calculate the CT between drug molecules and the MoS_2 monolayer. As depicted in Table 5, based on the Mulliken population, 0.01 and 0.010 and 0.121 e have been transferred from CFX and MTZ to MoS_2 monolayer, respectively. The results show also that the MoS_2 sheet gains electrons and drugs molecules lose electrons during the adsorption process. In other words, MoS_2 behaves as an acceptor, and drug molecules act as donor counterpart. There is a negligible CT between the MoS_2 and drug molecules, demonstrating that there is a weak interaction between drugs and MoS_2 nanosheet. To better understand the modification of the electronic structures of the pure MoS_2 monolayer and drug molecules' adsorptions on the MoS_2 monolayer, the electronic DOS diagrams were computed and plotted (Fig. 8).

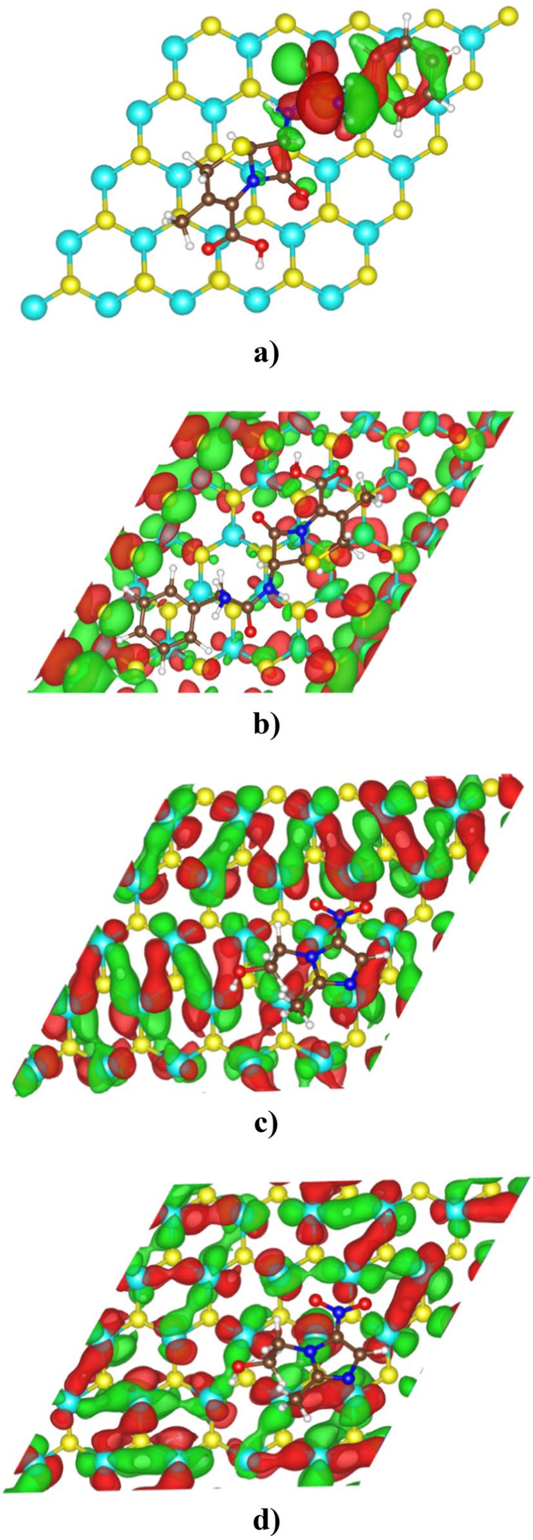

Fig. 9 The evaluated orbital localized **a** HOMO, **b** LUMO of CFX/MoS_2 complex and **c** HOMO **d** LUMO of MTZ/MoS2 system. (Red color denotes negative sign and green color indicates the positive sign of the wave function). (0.02 a.u. was employed as the iso-value for the total electron density)

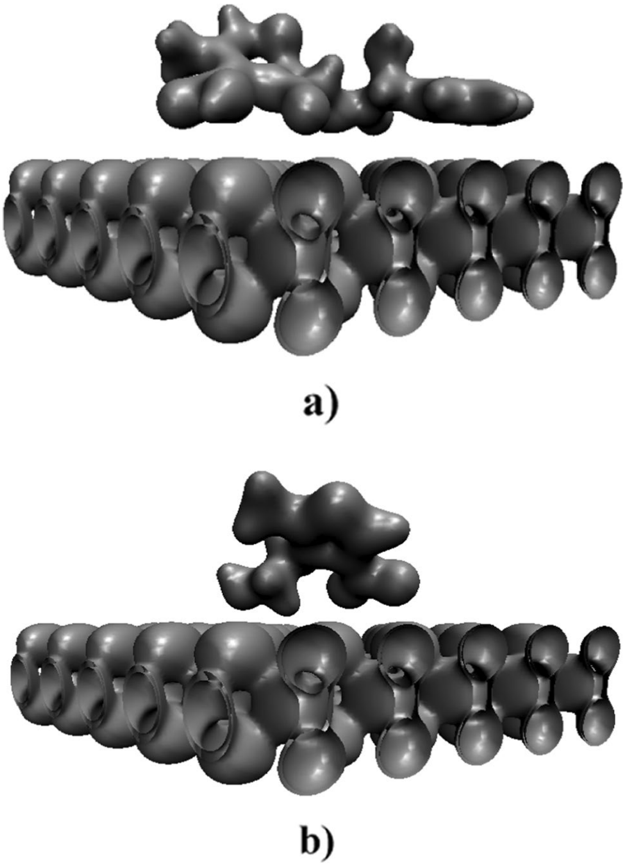

Fig. 10 The obtained total charge density for optimized **a** CFX/MoS_2 and **b** MTZ/MoS_2 systems. (0.05 a.u. was employed as the iso-value for the total electron density)

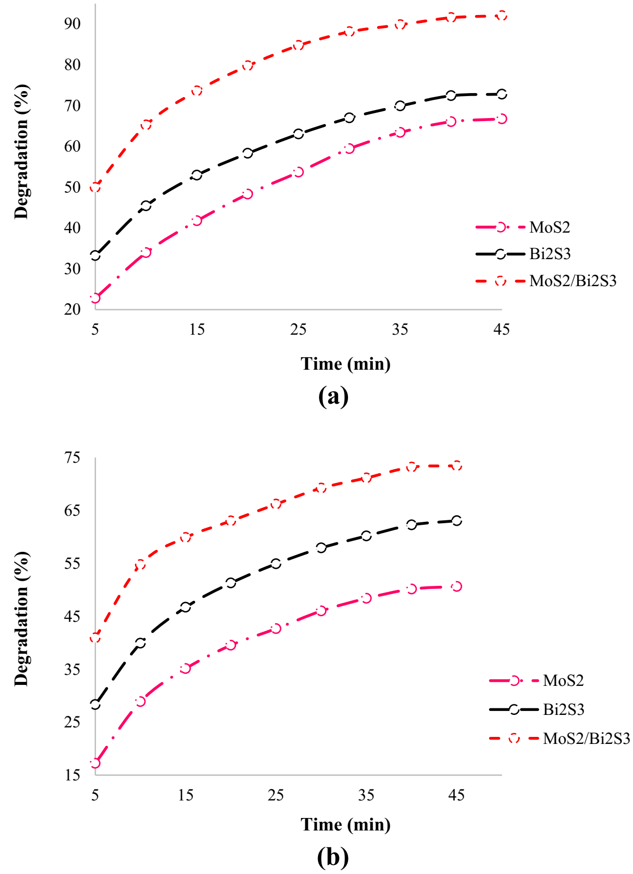

Fig. 11 **a** Photocatalytic degradation of MTZ by MoS_2, Bi_2S_3, and MoS_2/Bi_2S_3. **b** Photocatalytic degradation of CFX by MoS_2, Bi_2S_3, and MoS_2/Bi_2S_3

In electronic DOS plots, the E_g mentions the energy difference between the valence and the conduction levels. The electronic DOS graphs demonstrate that for selected complexes when the drugs interact with the monolayer surface, the band gap decreases compared to pure MoS_2. In other words, the electronic features of the MoS_2 monolayer were altered after adsorption with drugs, where a reduction in the E_g values was evaluated (from 1.973 eV in the pure MoS_2 monolayer to 0.010 and 1.936 eV in states MTZ and CFX complexes, an alteration of 99.49 and 1.875%, respectively) (see Table 5). It can be concluded that the band gap significantly changes when the MTZ interacts with the monolayer surface. Moreover, the difference in the Fermi level of the MoS_2 ($E_F = -3.926$ eV), MoS_2/MTZ ($E_F = -2.915$ eV), and MoS_2/CFX ($E_F = -3.502$ eV) clearly shows a CT between MoS_2 and MoS_2/Drugs in the adsorption process. To further insight into the adsorption process of drugs on the MoS_2 monolayer, frontier molecular orbitals (FMO) including HOMO and LUMO are implemented. The HOMO denotes the ability to donate an electron and the LUMO as an electron acceptor represents the ability to obtain an electron. As shown in Fig. 9, the HOMO level for the MoS_2/CFX complex is mainly located on the CFX drug surface, while the LUMO state is localized on the MoS_2 surface. In the case of the MoS_2/MTZ complex, both the HOMO and LUMO states are only focused on the MoS_2 sheet as represented in Fig. 9. We also assessed the total electron density maps for mentioned complexes. As we can see from Fig. 10, there is an insignificant overlapping of electron clouds between the drug molecules and the MoS_2 monolayer. In other words, there is no evidence for hybridization between two involving molecules.

3.3 Degradation of MTZ and CFX

Sulfide semiconductors with a small band gap have high photocatalytic activity by starting absorption in the visible and NIR regions. NIR photothermic can effectively absorb light energy, resulting in light-to-heat conversion, thereby increasing the reaction temperature. When the temperature increases, the rate of photocatalytic oxidation increases. To investigate the effect of MoS_2, Bi_2S_3, and MoS_2/Bi_2S_3 on the degradation efficiency of antibiotics, MTZ and CFX

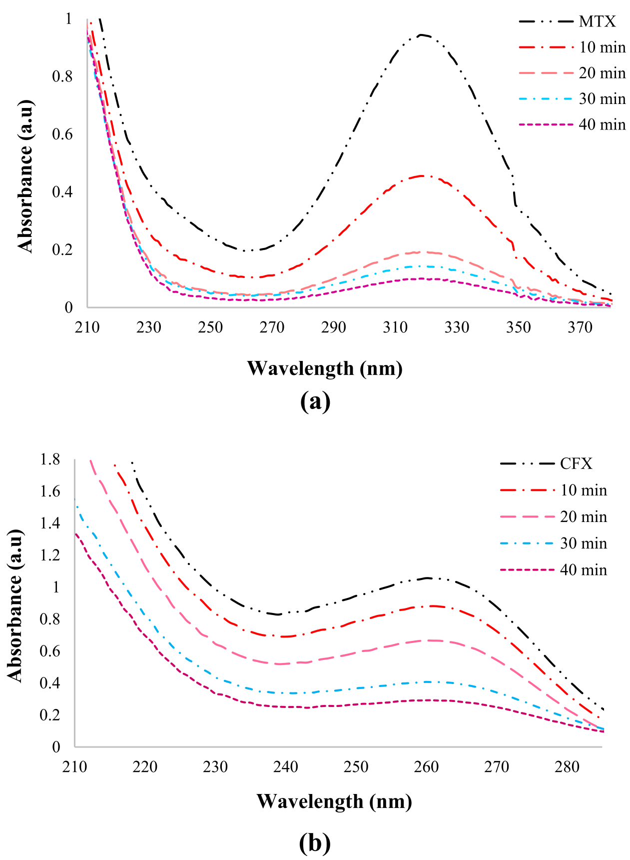

Fig. 12 **a** MTZ UV–Vis spectra before and after degradation. **b** CFX UV–Vis spectra before and after degradation

experiments were performed. According to the results, the performance of the Bi_2S_3 rod is higher than MoS_2 flower, which can be attributed to the high surface area of Bi_2S_3 rod 151.96 ($m^2\ g^{-1}$) and its small band gap of 1.18 eV. Among all the photocatalysts, the MoS_2/Bi_2S_3 heterostructure had the highest removal efficiency. It can be concluded that MoS_2/Bi_2S_3 heterostructure with a small band gap has high photocatalytic activity with absorption in the NIR region. Experimental results also showed that the degradation efficiency of MTZ is higher than that of CFX. Based on the results, the highest removal efficiencies of MTZ and CFX in 40 min and at pH 7 were obtained by MoS_2 flower/Bi_2S_3 rod photocatalyst, 91.54 and 73.18%, respectively (Fig. 11a, b). The results of optical degradation curves of MTZ ($\lambda = 319$ nm) and CFX ($\lambda = 261$ nm), before and after degradation for 10, 20, 30, and 40 min, are shown in Fig. 12a, b. Based on the results, after 40 min, the absorption of MTZ and CFX has decreased, which can be concluded that MTZ and CFX have been removed from the aqueous media.

3.4 Proposed mechanism of degradation of MTZ and CFX

Several intermediates in the photocatalytic degradation pathways of MTZ and CFX are suggested. Possible photocatalytic degradation pathways for MTZ and CFX are plotted and shown in Fig. 13a, b. For the MTZ photocatalytic degradation pathway, intermediate (I) is related to oxidation and decarboxylation. In addition, N-denitration and hydroxylation lead to the formation of product (III). In CFX, intermediate (I) is created due to ring opening by hydroxylation and demethylation due to $OH^{\cdot}/O_2$ attack on CFX and methyl exchange with hydroxyl. Decarboxylation and dealkylation can lead to the formation of a product (IV). Intermediate (V) output is due to CFX fragmentation. Deamination and oxidation of intermediate (V) lead to the production of the product (VI). Carboxylation and dealkylation form intermediate (II) and product (III). Previous researchers have suggested similar products for MTZ and CFX [64].

3.5 Recycled MoS_2/Bi_2S_3 photocatalyst

Because the possibility of reusing the synthesized photocatalyst is economically important, therefore, it is necessary to evaluate the efficiency of the MoS_2/Bi_2S_3 photocatalyst during successive recycling. The results obtained after five times recycling and reuse showed that MoS_2/Bi_2S_3 photocatalyst decreased its photocatalytic activity by increasing the recycling frequency, the results of which are shown in Fig. 14a, b.

3.6 Antibacterial activities

In this study, the antibacterial properties of the synthesized particles were investigated. The results showed that disks loaded with a different solution of Bi_2S_3, MoS_2, and MoS_2/Bi_2S_3 particles under NIR light irradiation have antibacterial properties, and the highest antibacterial activity was found in MoS_2/Bi_2S_3 particles under NIR irradiation. Based on the results, the inhibition rate for *E. coli* bacteria by the Bi_2S_3, MoS_2, and MoS_2/Bi_2S_3 particles under NIR light irradiation was recorded 2.6, 3.2, and 6.1 mm, respectively. The inhibition rate for *E. coli* bacteria by the Bi_2S_3, MoS_2, and MoS_2/Bi_2S_3 particles without NIR light irradiation was recorded 1.8, 2.7, and 4.8 mm, respectively (Table 6) [65]. The increase in temperature destroys bacterial membranes and proteins, and as a result, it leads to the inactivation of bacteria. Due to synergy, MoS_2/Bi_2S_3 particles have a higher ROS production capacity and more antibacterial properties (Fig. 15a, b).

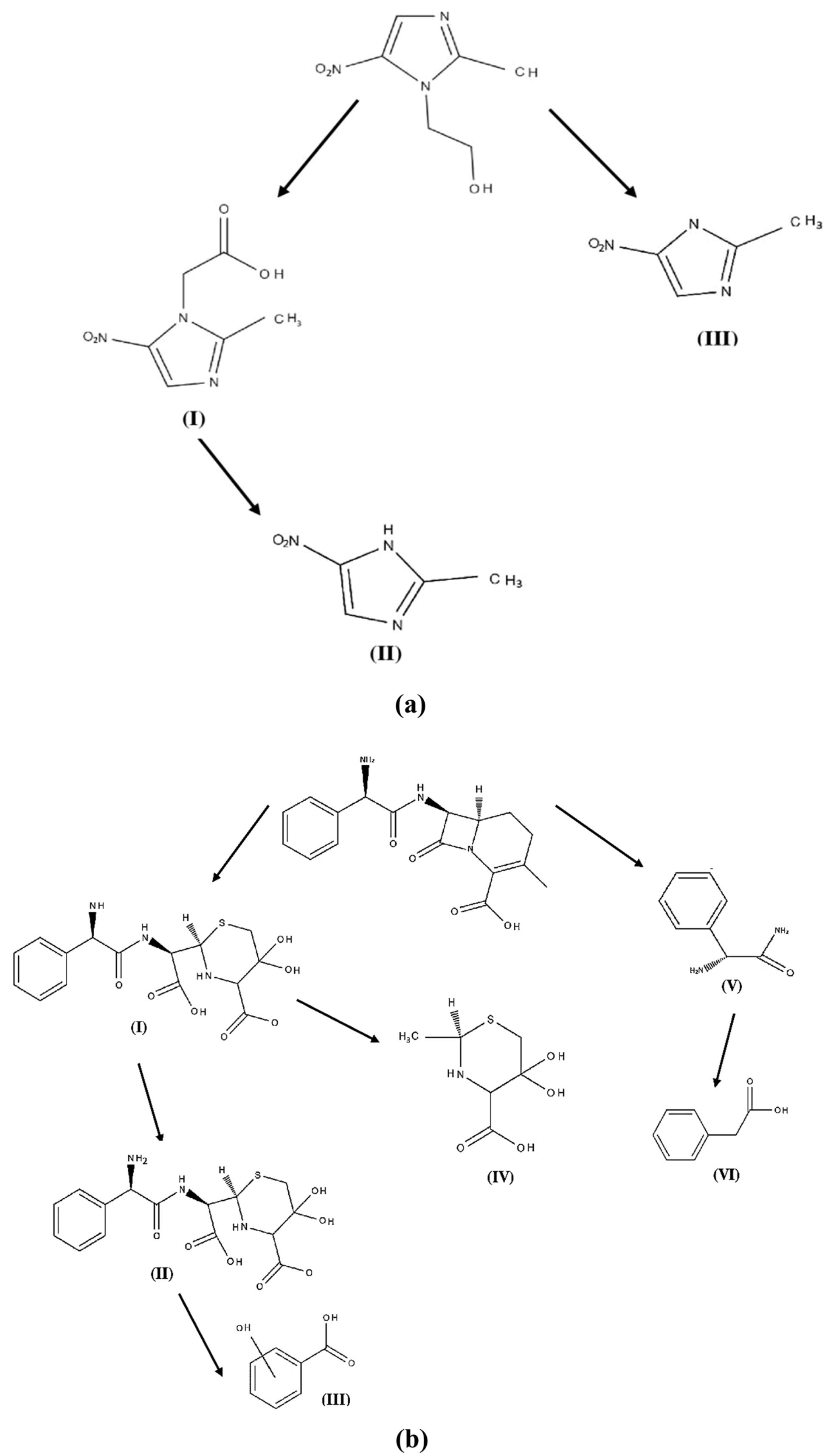

Fig. 13 **a** Proposed degradation pathways for MTZ. **b** Proposed degradation pathways for CFX

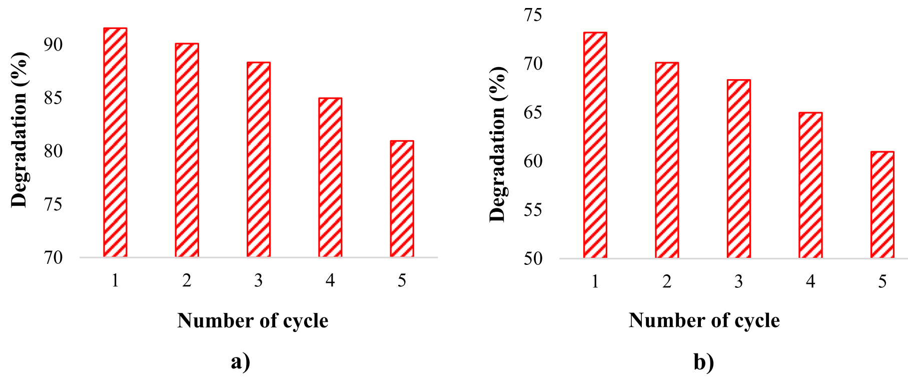

Fig. 14 Recycled photocatalytic degradation of **a** MTZ and **b** CFX

Table 6 Diameter of inhibition zone of Bi_2S_3, MoS_2, and MoS_2/Bi_2S_3 particles under and without NIR light

Sample	Diameter of inhibition zone (mm)
Bi_2S_3 (under NIR light)	2.6
MoS_2 (under NIR light)	3.2
MoS_2/Bi_2S_3 (under NIR light)	6.1
Bi_2S_3 (without NIR light)	1.8
MoS_2 (without NIR light)	2.7
MoS_2/Bi_2S_3 (without NIR light)	4.8

Based on the results obtained from this research, it can be concluded that the photocatalytic degradation of MTZ and CFX drugs under NIR light can be done with the lowest amount of photocatalyst consumed (0.02 g) in 40 min. Also, MoS_2/Bi_2S_3 particles showed acceptable antibacterial properties under NIR light irradiation.

4 Conclusion

MoS_2 flower-like and Bi_2S_3 rod-like were synthesized by hydrothermal method. Then, Bi_2S_3 rod was loaded on the MoS_2 flower. MoS_2, Bi_2S_3, and MoS_2/Bi_2S_3 particles were

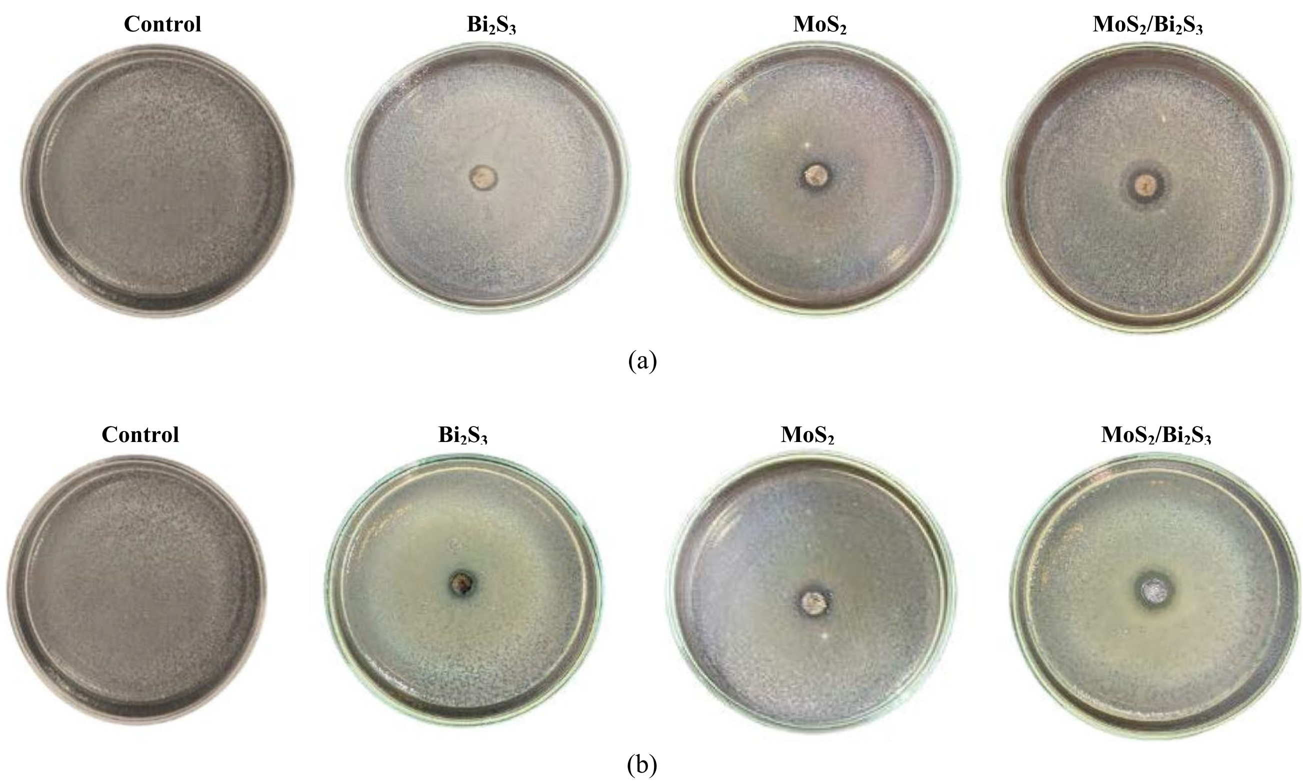

Fig. 15 **a** Photographs of colonies of *E. coli* after incubations with Bi_2S_3, MoS_2, and MoS_2/Bi_2S_3 under NIR light. **b** Photographs of colonies of *E. coli* after incubations with Bi_2S_3, MoS_2, and MoS_2/Bi_2S_3 without NIR light

characterized by different techniques. Degradation of MTZ and CFX were investigated onto MoS_2, Bi_2S_3, and MoS_2/Bi_2S_3 particles under NIR light. Based on the experimental results, the degradation efficiency of MTZ was higher than that of CFX. Also, the highest removal efficiencies of MTZ and CFX in 40 min and at pH 7 were obtained by MoS_2 flower/Bi_2S_3 rod photocatalyst, 91.54 and 73.18%, respectively. Based on the results, it can be concluded that the MoS_2/Bi_2S_3 photocatalyst has an acceptable performance in the removal of antibiotics. Based on the theoretical outcomes, the MoS_2 nanosheet can be used as the appropriate platform for the removal of mentioned antibiotics drugs, especially MTZ. The obtained results reveal that the E_g of MoS_2 was changed after the adsorption of antibiotic drugs. It can be concluded that the E_g significantly changes when the MTZ interacts with the MoS_2 nanosheet. Also, in this study, the antibacterial properties of the synthesized particles were investigated. The results showed that the particles of Bi_2S_3, MoS_2, and MoS_2/Bi_2S_3 under NIR light irradiation have antibacterial properties, and the highest antibacterial property is related to the MoS_2/Bi_2S_3 sample under NIR irradiation. In the present work, MoS_2/Bi_2S_3 photocatalyst with antibacterial properties was made for the first time, which is a simple, cost-effective and environmentally friendly technique that has high efficiency for the degradation of antibiotics from aquatic environments.

Author contributions Methodology, data collection, formal analysis, writing—original draft preparation, and writing—review and editing were performed by HP, NEF, and MR. Software and validation were carried out by MR. All authors have read and agreed to the published version of the manuscript.

Availability of data and materials All data will be available if required.

Declarations

Conflict of interest The authors declare that they have no known competing financial interests or personal relationships that could have appeared to influence the work reported in this paper.

Ethics approval We approved all ethics.

References

1. S.S. Fekra, N.E. Fard, R. Fazaeli, Photocatalytic degradation of antibiotic norfloxacin aqueous solution by Ce/Bi_2WO_6: optimization and simulation of process by RSM. Russ. J. Appl. Chem. **94**(6), 824–834 (2021)
2. M. Amanulla, C.M. Magdalane, G. Ramalingam, R. Sundaram, N. Tamam, H.H. Somaily, M.S. Al-Buriahi, Fabrication and characterization of Th $(MoO_4)_2/TiO_2$ nanocomposite for potential use in photocatalytic degradation of toxic pollutants. Appl. Phys. A. **128**(5), 1–21 (2022)
3. N. Askari, M. Farhadian, D. Mowla, M. Beheshti, Evaluating the binary Z-scheme $Bi_2S_3/CuWO_4$ immobilized on FTO as a visible-light-driven photocatalyst for metronidazole degradation-response surface method. Appl. Phys. A. **127**(10), 1–13 (2021)
4. M. Qian, L. Yang, X. Chen, K. Li, W. Xue, Y. Li, G. Shen, The treatment of veterinary antibiotics in swine wastewater by biodegradation and Fenton-like oxidation. Sci. Total Environ. **710**, 136299 (2020)
5. N. Nasseh, F.S. Arghavan, S. Rodriguez-Couto, A.H. Panahi, M. Esmati, T.J.A. Musawi, Preparation of activated carbon@ ZnO composite and its application as a novel catalyst in catalytic ozonation process for metronidazole degradation. Adv. Powder. Technol. **31**(2), 875–885 (2020)
6. B.M. Lee, L.K. Harold, D.V. Almeida, L. Afriat-Jurnou, H.L. Aung, B.M. Forde, C.J. Jackson, Predicting nitroimidazole antibiotic resistance mutations in Mycobacterium tuberculosis with protein engineering. PLoS Pathog. **16**(2), e1008287 (2020)
7. A. Eguchi, S. Mizukami, M. Nakamura, S. Masuda, H. Murayama, M. Kawashima, T. Yoshida, Metronidazole enhances steatosis-related early-stage hepatocarcinogenesis in high fat diet-fed rats through DNA double-strand breaks and modulation of autophagy. Environ. Sci. Pollut. Res. **29**(1), 779–789 (2022)
8. A. Nasiri, S. Rajabi, M. Hashemi, H. Nasab, $CuCoFe_2O_4$@ MC/AC as a new hybrid magnetic nanocomposite for metronidazole removal from wastewater: Bioassay and toxicity of effluent. Sep. Purif. Technol. **296**, 121366 (2022)
9. Q. Wang, S. Tu, W. Wang, W. Chen, X. Duan, L. Chang, Optimized Indium modified Ti/PbO_2 anode for electrochemical degradation of antibiotic cefalexin in aqueous solutions. Colloids Surf. A Physicochem. Eng. **628**, 127244 (2021)
10. P. Chaturvedi, P. Shukla, B.S. Giri, P. Chowdhary, R. Chandra, P. Gupta, A. Pandey, Prevalence and hazardous impact of pharmaceutical and personal care products and antibiotics in environment: A review on emerging contaminants. Environ. Res. **194**, 110664 (2021)
11. N. Elmi Fard, R. Fazaeli, Fabrication of superhydrophobic $CoFe_2O_4$/polyaniline/covalent organic frameworks/cotton fabric membrane and evaluation of its efficiency in separation of olive oil from water. J. Chin. Chem. Soc. **69**(12), 2014–2026 (2022)
12. N.E. Fard, R. Fazaeli, M. Yousefi, S. Abdolmohammadi, Oxidative Desulfurization of Dibenzothiophene Using M/TiO_2/MWW (M= Cu, Ag, and Au) Composite. Russ. J. Phys. Chem. **95**(1), S23–S32 (2021)
13. R. Fazaeli, N.E. Fard, Desulfurization of gasoline fuel via photocatalytic oxidation/adsorption using NaX zeolite-based under mild conditions: process optimization by central composite design. Russ. J. Appl. Chem. **93**(7), 973–982 (2020)
14. L. Hao, Y. Zhang, Q. Zhao, S. Guan, T. Hu, Y. Lu, Comparative study of MoS_2/MoO_3, g-C_3N_4/MoO_3 heterojunction films and their improved photocatalytic activity. Appl. Phys. A. **127**(10), 1–10 (2021)
15. N.E. Fard, R. Fazaeli, M. Yousefi, S. Abdolmohammadi, Morphology-controlled synthesis of CuO, CuO Rod/MWW composite for advanced oxidation of indole and benzothiophene. Chem. Select **4**, 9529–9539 (2019)
16. N.E. Fard, R. Fazaeli, M. Yousefi, S. Abdolmohammadi, Oxidation of carbazole by shape-controllable Cu_2O on MWW catalysis. Appl. Phys. A. **125**(9), 1–15 (2019)
17. N.E. Fard, R. Fazaeli, Optimization of operating parameters in photocatalytic activity of visible light active Ag/TiO_2 nanoparticles. Russ. J. Phys. Chem. **92**(13), 2835–2846 (2018)
18. N.E. Fard, R. Fazaeli, A novel kinetic approach for photocatalytic degradation of azo dye with CdS and Ag/CdS nanoparticles fixed on a cement bed in a continuous-flow photoreactor. Int. J. Chem. Kinet. **48**(11), 691–701 (2016)
19. S. Abdolmohammadi, S.R. Nasrabadi, A. Seif, N.E. Fard, Ag/CdS nanocomposite: an efficient recyclable catalyst for the synthesis of novel 8-aryl-8H-[1, 3] dioxolo [4, 5-g] chromene-6-carboxylic

acids under mild reaction conditions. Comb. Chem. High Throughput Screen. **21**(5), 323–328 (2018)
20. N.E. Fard, R. Fazaeli, R. Ghiasi, Band gap energies and photocatalytic properties of CdS and Ag/CdS nanoparticles for Azo dye degradation. Chem. Eng. Technol. **39**(1), 149–157 (2016)
21. A. Butkovskyi, A.H. Faber, Y. Wang, K. Grolle, R. Hofman-Caris, H. Bruning et al., Removal of organic compounds from shale gas flowback water. Water Res. **138**, 47–55 (2018)
22. C.Z. Ning, L. Dou, P. Yang, Bandgap engineering in semiconductor alloy nanomaterials with widely tunable compositions. Nat. Rev. Mater. **2**(12), 1–14 (2017)
23. Z. Wang, B. Mi, Environmental applications of 2D molybdenum disulfide (MoS_2) nanosheets. Environ. Sci. Technol. **51**(15), 8229–8244 (2017)
24. X. Wang, J. He, L. Mao, X. Cai, C. Sun, M. Zhu, CsPbBr 3 perovskite nanocrystals anchoring on monolayer MoS2 nanosheets for efficient photocatalytic CO2 reduction. Chem. Eng. J. **416**, 128077 (2021)
25. E. Benavente, F. Duran, C. Sotomayor-Torres, G. Gonzalez, Heterostructured layered hybrid ZnO/MoS_2 nanosheets with enhanced visible light photocatalytic activity. J. Phys. Chem. Solids. **113**, 119–124 (2018)
26. S. Liu, D. Chi, Q. Zou, Y. Ma, R. Chen, K. Zhang, MOFs-derived MoS_2/C_3N_4 composites with highly efficient charge separation for photocatalytic H_2 evolution. Inorganica. Chim. Acta **533**, 120787 (2022)
27. A. Nipane, D. Karmakar, N. Kaushik, S. Karande, S. Lodha, Few-layer MoS_2 p-type devices enabled by selective doping using low energy phosphorus implantation. ACS Nano **10**(2), 2128–2137 (2016)
28. X. Zhang, X. Huang, M. Xue, X. Ye, W. Lei, H. Tang, C. Li, Hydrothermal synthesis and characterization of 3D flower-like MoS_2 microspheres. Mater. Lett. **148**, 67–70 (2015)
29. G. Jiang, X. Zhang, C. Liu, H. Ma, H. Yu, F. Wang, First-principles investigation on the vacancy dependence on the optical and electronic properties of Bi_2S_3 semiconductor ceramics. Vacuum **181**, 109759 (2020)
30. R. Fortulan, S. Aminorroaya Yamini, C. Nwanebu, S. Li, T. Baba, M.J. Reece, T. Mori, Thermoelectric performance of n-type magnetic element doped Bi_2S_3. ACS Appl. Energy Mater **5**(3), 3845–3853 (2022)
31. B. Weng, X. Zhang, N. Zhang, Z.R. Tang, Y.J. Xu, Two-dimensional MoS_2 nanosheet-coated Bi_2S_3 discoids: synthesis, formation mechanism, and photocatalytic application. Langmuir **31**(14), 4314–4322 (2015)
32. D.C. Onwudiwe, V.M. Nkwe, Morphological variations in Bi_2S_3 nanoparticles synthesized by using a single source precursor. Heliyon **6**(7), e04505 (2020)
33. C. Zhang, D. Li, P. Pei, W. Wang, B. Chen, Z. Chu et al., Rod-based urchin-like hollow microspheres of Bi_2S_3: facile synthesis, photo-controlled drug release for photoacoustic imaging and chemo-photothermal therapy of tumor ablation. Biomaterials **237**, 119835 (2020)
34. M. Li, J. Wang, P. Zhang, Q. Deng, J. Zhang, K. Jiang, J. Chu, Superior adsorption and photoinduced carries transfer behaviors of dandelion-shaped Bi_2S_3@ MoS_2: experiments and theory. Sci. Rep. **7**(1), 1–14 (2017)
35. W. Fei, H. Li, N. Li, D. Chen, Q. Xu, H. Li, J. Lu, Facile fabrication of ZnO/MoS_2 pn junctions on Ni foam for efficient degradation of organic pollutants through photoelectrocatalytic process. Sol. Energy **199**, 164–172 (2020)
36. L. Luo, X. Shen, L. Song, Y. Zhang, B. Zhu, J. Liu et al., MoS_2/Bi_2S_3 heterojunctions-decorated carbon-fiber cloth as flexible and filter-membrane-shaped photocatalyst for the efficient degradation of flowing wastewater. J. Alloys Compd. **779**, 599–608 (2019)
37. Y.R. Reynoso, A. Martinez-Ayala, M. Pal, F. Paraguay-Delgado, N.R. Mathews, Bi_2S_3 nanoparticles by facile chemical synthesis: Role of pH on growth and physical properties. Adv Powder Technol. **29**(12), 3561–3568 (2018)
38. P. Hohenberg, W. Kohn, Inhomogeneous electron gas. Phys. Rev. **136**(3B), B864 (1964)
39. J.R. Moreno, C. Giuseppe, G. Antoine, Deep learning the hohenberg-kohn maps of density functional theory. Phys Rev Lett. **125**(7), 076402 (2020)
40. A. García, N. Papior, A. Akhtar, E. Artacho, V. Blum, E. Bosoni, P. Brandimarte, M. Brandbyge, J.L. Cerdá, F. Corsetti, R. Cuadrado, Siesta: Recent developments and applications. J Chem Phys **152**(20), 204108 (2020)
41. J.M. Soler, E. Artacho, J.D. Gale, A. García, J. Junquera, P. Ordejón, D. Sánchez-Portal, The SIESTA method for ab initio Order-N materials simulation. J. Condens. Matter Phys. **14**(11), 2745 (2002)
42. J.P. Perdew, K. Pbe, M. Ernzerhof, Generalized gradient approximation made simple. Phys. Rev Lett. **77**(18), 3865 (1996)
43. A. Aghahosseinin, L. Edjlali, S. Jamehbozorgi, M. Rezvani, E. Ghasemi, Theoretical investigations of functionalization of graphene and ZnO monolayers with mercaptopurine at aqueous media: a dispersion-corrected DFT calculations and molecular dynamic simulations. J. Mol. Liq. **369**, 120865 (2023)
44. S. Tanreh, M. Rezvani, M. Darvish Ganji, Molecular simulation investigations on interaction properties of the teriflunomide–chitosan complex in aqueous solution. J Phys Chem Solids **174**, 111171 (2023)
45. M. Sabet, S. Tanreh, A. Khosravi, M. Astaraki, M. Rezvani, M. Darvish Ganji, Theoretical assessment of the solvent effect on the functionalization of Au_{32} and C_{60} nanocages with fluorouracil drug. Diam. Relat. Mater. **126**, 109142 (2022)
46. M. TaleMoghim, S. Jamehbozorgi, M. Rezvani, M. Ramezani, Computational investigation on the geometry and electronic structures and absorption spectra of metal-porphyrin-oligo- phenyleneethynylenes-[60] fullerene triads. Spectrochim. Acta A Mol. Biomol **280**, 121488 (2022)
47. H. Li, M. Huang, G. Cao, Magnetic properties of atomic 3d transition-metal chains on S-vacancy-line templates of monolayer MoS_2: Effects of substrate and strain. J. Mater. Chem. C. **5**(18), 4557–4564 (2017)
48. A. Kumar, D. Banyai, P.K. Ahluwalia, R. Pandey, S.P. Karna, Electronic stability and electron transport properties of atomic wires anchored on the MoS_2 monolayer. Phys. Chem. Chem. Phys **16**(37), 20157–20163 (2014)
49. N. Troullier, J.L. Martins, Efficient pseudopotentials for plane-wave calculations. Phys. Rev. B Condens. Matter **43**(3), 1993 (1991)
50. Q. Zhang, T. Çağın, A. van Duin, W.A. Goddard, Y. Qi, L.G. Hector, Adhesion and nonwetting-wetting transition in the Al/$\alpha-Al_2O_3$ interface. Phys. Rev. B **694**, 4 (2004)
51. R.P. Feynman, Forces in molecules. Phys. Rev. **56**(4), 340 (1939)
52. H.J. Monkhorst, J.D. Pack, Special points for Brillouin-zone integrations. Phys. Rev. B **13**(12), 5188 (1976)
53. S. Grimme, J. Antony, S. Ehrlich, H. Krieg, J. Chem. Phys. **132**, 154104 (2010)
54. T. Ozaki, K. Nishio, H. Kino, Efficient implementation of the nonequilibrium Green function method for electronic transport calculations. Phys. Rev. B **8**, 035116 (2010)
55. K. Lejaeghere, G. Bihlmayer, T. Björkman, P. Blaha, S. Blügel, V. Blum, D. Caliste, I.E. Castelli, S.J. Clark, A. Dal Corso, S. de Gironcoli, T. Deutsch, J.K. Dewhurst, I. Di Marco, C. Draxl, M. Dułak, O. Eriksson, J.A. Flores-Livas, K.F. Garrity, L. Genovese et al., Science **351**, aad3000 (2016)
56. G. Hashemkhani Shahnazari, M. Darvish Ganji, Understanding structural and molecular properties of complexes of nucleobases

and Au13 golden nanocluster by DFT calculations and DFT-MD simulation. Sci Rep **11**, 435 (2021)
57. T. Ozaki, H. Kino, Efficient projector expansion for the ab initio LCAO method. Phys. Rev. B **72**(4), 045121 (2005)
58. R.S. Mulliken, Electronic population analysis on LCAO–MO molecular wave functions. I. The J. Chem. Phys **23**(10), 1833–1840 (1995)
59. P. Niknam, S. Jamehbozorgi, M. Rezvani, V. Izadkhah, understanding delivery and adsorption of Flutamide drug with ZnONS based on: dispersion-corrected DFT calculations and MD simulations. Physica E **135**, 114937 (2022)
60. C. Li, B. Fan, W. Li, L. Wen, Y. Liu, T. Wang, Y. Yin, Bandgap engineering of monolayer MoS_2 under strain: a DFT study. J. Korean. Phys. Soc **66**(11), 1789–1793 (2015)
61. Y. Li, Z. Zhou, S. Zhang, Z. Chen, MoS_2 nanoribbons: high stability and unusual electronic and magnetic properties. J. Am. Chem. Soc. **130**(49), 16739–16744 (2008)
62. Q. Yue, J. Kang, Z. Shao, X. Zhang, S. Chang, G. Wang et al., Mechanical and electronic properties of monolayer MoS_2 under elastic strain. Phys. Lett. A **376**(12–13), 1166–1170 (2012)
63. A. Miralrio, E.R. Cortes, M. Castro, Electronic properties and enhanced reactivity of MoS_2 monolayers with substitutional gold atoms embedded into sulfur vacancies. Appl. Sur. Sci **455**, 758–770 (2018)
64. N. Askari, M. Beheshti, D. Mowla, M. Farhadian, Facile construction of novel Z-scheme $MnWO_4/Bi_2S_3$ heterojunction with enhanced photocatalytic degradation of antibiotics. Mater. Sci. Semicond. Process. **127**, 105723 (2021)
65. A.A.R. Niema, E.M. Abbas, N.K. Abdalameer, Enhanced antibacterial activity of selenium nanoparticles prepared by cold plasma in liquid. Dig. J. Nanomater. Biostruct. (DJNB) **16**(4), 1479 (2021)

Authors and Affiliations

Hoda Pasdar[1] · Narges Elmi Fard[2] · Mahyar Rezvani[3]

Narges Elmi Fard
nargeselmi@yahoo.com

Mahyar Rezvani
mahyar.rezvani@gmail.com

[1] Department of Chemistry, North Tehran Branch, Islamic Azad University, Tehran, Iran

[2] Department of Chemistry, Science and Research Branch, Islamic Azad University, Tehran, Iran

[3] Department of Nanochemistry, Faculty of Pharmaceutical Chemistry, Tehran Medical Sciences, Islamic Azad University, Tehran, Iran